RSC Advances

ROYAL SOCIETY
OF CHEMISTRY

PAPER

View Article Online
View Journal | View Issue

Cite this: *RSC Adv.*, 2022, **12**, 17182

Manganese oxide nanorod catalysts for low-temperature selective catalytic reduction of NO with NH_3

Yifan Wang, Yanli Wang,* Zhenkai Kong, Ying Kang and Liang Zhan *

Received 8th September 2021
Accepted 31st March 2022

DOI: 10.1039/d1ra06758c

rsc.li/rsc-advances

MnO_x nanorod catalysts were successfully synthesized by two different preparation methods using porous SiO_2 nanorods as the template and investigated for the low-temperature selective catalytic reduction (SCR) of NO with NH_3. The catalysts were characterized by scanning electron microscopy, transmission electron microscopy, nitrogen adsorption, X-ray diffraction, X-ray photoelectron spectroscopy, and NH_3 temperature-programmed desorption. The results show that the obtained MnO_x-P nanorod catalyst prepared by redox precipitation method exhibits higher NO removal activity than that prepared by the solvent evaporation method in the low temperature range of 100–180 °C, where about 98% NO conversion is achieved over MnO_x(0.36)-P nanorods. The reason is mainly attributed to MnO_x(0.36)-P nanorods possessing unique flower-like morphology and mesoporous structures with high pore volume, which facilitates the exposure of more active sites of MnO_x and the adsorption of reactant gas molecules. Furthermore, there is a lower crystallinity of MnO_x, higher percentage of Mn^{4+} species and a large amount of strong acid sites on the surface. These factors contribute to the excellent low-temperature SCR activity of MnO_x(0.36)-P nanorods.

1. Introduction

Nitrogen oxides (NO_x) are considered to be one of the main air pollutants, which can cause great harm to the ecological environment and human health. Therefore, it is urgent to control the emissions of NO_x. The selective catalytic reduction (SCR) of NO with NH_3 has been proven to be the most effective technology for the removal of NO_x. Commercial SCR catalysts, V_2O_5–WO_3/TiO_2 and V_2O_5–MoO_3/TiO_2 catalysts have shown high activity of NO removal, and these catalysts must be used in the temperature range of 350–450 °C.[1,2] To satisfy the high operating temperature, the SCR unit needs to be placed upstream of the electrostatic precipitator and desulfurization devices, resulting in the deactivation of catalysts because of high concentration of dust and SO_2 in the flue gases. In order to overcome the disadvantages of these V_2O_5/TiO_2 based catalysts, researchers have paid much attentions on developing efficient low-temperature SCR catalysts, which can be placed downstream of the desulfurizer and electrostatic precipitators without the need for reheating of flue gases.[3–5]

Various transition metal oxide catalysts have been found to be active in the NH_3-SCR reaction. Among them, manganese oxide (MnO_x) catalysts exhibit excellent low temperature-SCR activities due to their variable valence states and high redox properties.[6,7] In addition, it has been demonstrated that the specific surface area and crystallinity of MnO_x have also great influence on their SCR activities.[8] Furthermore, it has been reported that the morphologies of the catalysts significantly influence their properties and catalytic performance.[9–11] Recently, mesoporous materials have attracted extensive attention owing to their large specific surface area, highly ordered mesoporous structure, which are advantageous to the generation of abundant active sites and mass transport of gas molecules. In particular, mesoporous metal oxides combine the advantages of both metal oxides and mesoporous structure in comparison with nanoparticles, which have found applications in various fields, such as electrode materials, gas sensors and adsorption, catalysis, *etc.*[12–14] For instance, Gao *et al.*[15] reported a three-dimensional (3D) mesoporous MnO_2 prepared using KIT-6 as a template, which showed much higher SCR activity than mesoporous MnO_2 templated from SBA-15 or MCM-41, maintaining NO conversion of 100% in the temperature range of 75–275 °C, because of the special 3D mesostructure. Tian *et al.*[16] studied MnO_2 nanorods exhibited higher NO conversion than MnO_2 nanotubes and nanoparticles, and found that the higher SCR activity of MnO_2 nanorods may be mainly attributed to lower crystallinity, more lattice oxygen, higher reducibility, and more amount of strong acid sites. Therefore, controlled synthesis of MnO_x catalysts with different morphologies is very effective way to improve their SCR activities. However, there are still many challenges.

State Key Laboratory of Chemical Engineering, Key Laboratory for Specially Functional Polymers and Related Technology of Ministry of Education, Shanghai Key Laboratory of Multiphase Materials Chemical Engineering, East China University of Science and Technology, Shanghai 200237, China. E-mail: zhanliang@ecust.edu.cn; Fax: +86 21 64252914; Tel: +86 21 64252924

In this work, we synthesized a series of MnO_x nanorods catalysts using porous SiO_2 nanorods as template through two different preparation methods. The activities of these MnO_x nanorods catalysts for SCR of NO at low temperatures were evaluated. The effect of Mn loading on SCR activities of MnO_x nanorods catalysts at different temperatures were also investigated. The catalysts were characterized to understand the structure and morphologies of MnO_x nanorods catalysts as well as their relationship with catalytic activity. The results are of importance for better understanding of low temperature SCR reaction on nanostructured MnO_x catalysts and beneficial to promote the development of NO removal technology from flue gases.

2. Experimental

2.1 Catalyst preparation

All the chemical reagents used were analytical grade. MnO_x nanorods catalysts were prepared by two-step process. Firstly, the porous SiO_2 nanorods template was synthesized according to the previously reported procedure.[17] Secondly, MnO_x nanorods catalysts were prepared by two different methods using the porous SiO_2 nanorods as template. Detailed preparation methods were the following:

2.1.1 Redox precipitation method (P). A series of MnO_x nanorods catalysts were synthesized by the redox precipitation method using $KMnO_4$ as oxidant and manganese acetate as reductant, respectively. In a typical synthesis, a certain amount of the as-synthesized porous SiO_2 nanorods was initially dispersed in 50 mL deionized water by ultrasonic treatment, subsequently appropriate amount of manganese acetate was slowly added to the above solution. After stirring for 6 h, the solution of $KMnO_4$ containing 40 mL deionized water was slowly added to the above mixture, and continuously stirred for 12 h. The main reaction between $Mn(CH_3COO)_2$ and $KMnO_4$ is expressed by the following equation: ($3Mn^{2+} + 2MnO_4^- + 2H_2O \rightarrow 5MnO_2 + 4H^+$). Then, the obtained product was collected by filtration, and washing several times with deionized water, and then drying at 110 °C for 12 h. Finally, the $SiO_2@MnO_x$ was treated with 2 M NaOH solution at 80 °C to remove the SiO_2 nanorods template, followed by centrifugation and washing with deionized water several times, drying at 110 °C for 12 h. The resultant catalysts are labeled as $MnO_x(y)$-P nanorods, where *y* represents the mass ratio of Mn to SiO_2 nanorods template, and P represents the redox precipitation method.

2.1.2 Solvent evaporation method (E). For comparison, the MnO_x nanorods catalysts were also synthesized by the solvent evaporation method using manganese acetate as the precursor. A certain amount of the as-synthesized porous SiO_2 nanorods was initially dispersed in 40 mL ethanol by ultrasonic treatment. Subsequently, appropriate amount of manganese acetate was slowly added to the above solution, and stirred for 2 h. Then, the mixture was heated up to 50 °C to evaporate the ethanol. The obtained product was dried at 80 °C for 12 h, followed by calcination at 400 °C for 3 h in air atmosphere. Finally, the SiO_2 nanorods template was removed with 2 M NaOH solution at 80 °C, then centrifugation, washing with deionized water several times and drying at 110 °C for 12 h. The resultant catalysts are labeled as $MnO_x(y)$-E nanorods, where *y* represents the mass ratio of Mn to SiO_2 nanorods template, and E represents the solvent evaporation method.

2.2 Activity test

NO removal activity tests were carried out in a fixed-bed reactor with a diameter of 8 mm. The gas mixture consisted of 500 ppm NO, 500 ppm NH_3, 5.0 vol% O_2 and balance N_2. In all experiments, the total gas flow rate was maintained at 500 mL min^{-1}, corresponding to a gas hourly space velocity (GHSV) of 62 000 h^{-1}. The reaction temperatures were controlled regulated from 100 to 300 °C. The concentrations of NO and O_2 in the inlet and outlet gases were continually measured on-line by a flue gas analyzer (MRU VARIO PLUS, Germany).

2.3 Characterization

The morphologies and microstructures of the samples were examined using scanning electron microscope (SEM, FEI Nova NanoSEM 450) and transmission electron microscopy (TEM, JEOL JEM-2100F). The pore structure was measured at 77 K using a Quadrasorb SI analyzer (Quantachrome Instrument Crop) and the corresponding pore size distribution was obtained by the density functional theory (DFT model). X-ray diffraction (XRD) measurements were recorded on a Rigaku D/max 2550 diffractometer using Cu Kα radiation. X-ray photoelectron spectroscopy (XPS) measurements were carried out on an Axis Ultra DLD spectrometer with Al Kα radiation. NH_3-temperature programmed desorption (NH_3-TPD) was performed on a TP-5080 adsorption analyzer (Xianquan Co.) with a thermal conductivity detector (TCD). Before the NH_3-TPD experiment, 0.1 g sample was pretreated in He flow at 300 °C for 30 min, followed by cooling down to 100 °C. Afterwards, the He flow was switched to a stream containing 5 vol% NH_3/He to adsorb NH_3 for 60 min at 100 °C and then purged with He at the same temperature. Finally, the temperature was increased to 800 °C in He flow at a heating rate of 10 °C min^{-1}.

3. Results and discussion

3.1 Morphological characterization

Fig. 1 shows SEM images of the porous SiO_2 nanorods. As can be observed in Fig. 1, the obtained SiO_2 nanorods shows one-

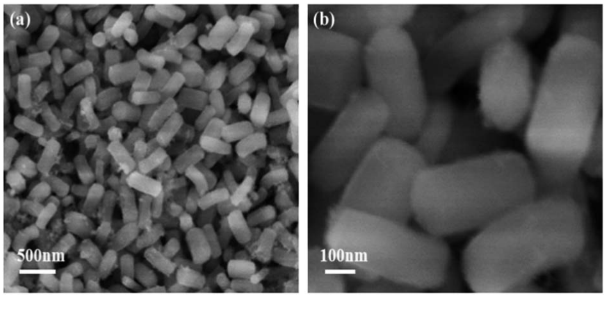

Fig. 1 SEM images of the porous SiO_2 nanorods.

dimensional rod-like structure. These nanorods are nearly uniform with lengths in the range of 300–400 nm and diameters of about 100–200 nm. Furthermore, all SiO_2 nanorods are almost monodispersed without aggregation.

The morphologies and microstructures of MnO_x nanorods catalysts prepared by different methods are characterized by SEM. The results in Fig. 2 indicate the different morphology can be clearly observed over MnO_x(0.36)-E and MnO_x(0.36)-P nanorods. After the loading of MnO_x and etching by the NaOH solution, the morphology of MnO_x(0.36)-E nanorods is mainly one-dimensional rod-like structure, which does not change much compared with that of SiO_2 nanorods. These indicate that MnO_x is uniformly distributed in the rod-like structure, favorable to the enhancement of SCR activity. Additionally, a small amount of nanoparticles and nanosheets MnO_x are observable on the surface of the rod-like structure, which may be caused by the unloaded MnO_x on the SiO_2 nanorods because of the precipitation and crystallization of partial manganese precursor during the solvent evaporation process. The SEM image of MnO_x(0.36)-P nanorods is clearly different from that of MnO_x(0.36)-E nanorods. Flower-like structure is observed, which is assembled by numerous manganese oxide nanosheets (Fig. 2c and d). After the careful observation, it is found that a certain amount of loose macroporous structure is also formed on the surface of the catalyst, due to the accumulation of MnO_x nanosheets. These macroporous structure could facilitate the adsorption and desorption of reactant gas molecules on the active sites of catalyst surface, which is advantageous to NH_3-SCR reaction.

The detailed morphologies and microstructures of MnO_x nanorods catalysts obtained by different methods are further characterized by TEM. From Fig. 3a, it is observed that MnO_x(0.36)-E nanorods still maintains one-dimensional rod-like structure, agreeing well with the SEM results. It is worth noting that the inter center of MnO_x(0.36)-E nanorods is not completely hollow structure. Since the porous SiO_2 nanorods has abundant mesoporous structures, it is reasonable to expect the manganese precursor easily fills the mesoporous template including the edge and inner pores of SiO_2 nanorods during the MnO_x impregnation process. Thus, the inner partially hollow structure is formed after the further etching of SiO_2. In addition, there exists unloaded nanoparticles and nanosheets MnO_x near the rod-like structure, in accordance with the SEM results (Fig. 2a and b). Compared to TEM image of MnO_x(0.36)-E nanorods, MnO_x(0.36)-P nanorods is mainly composed of nanorods, with a diameter about 100–200 nm and length about 300–500 nm (Fig. 3c), which is similar with the size of the SiO_2 nanorods. And it can also be seen that MnO_x nanosheets are deposited on the surface of the nanorods, suggesting that the flower-like MnO_x is assembled by these MnO_x nanosheets. Meanwhile, many porous structures in the inner space of nanorods are also observed, which is explained because the MnO_x nanosheets are self-assembled randomly and not parallel to each other, leading to the formation of the porous structure. Such results are good agreement with the SEM observation (Fig. 2c and d).

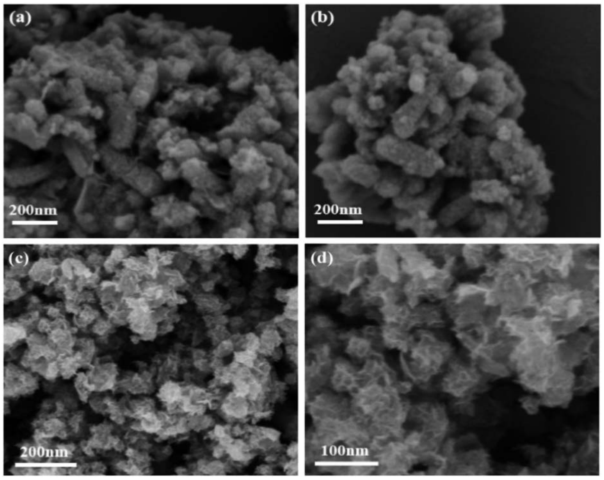

Fig. 2 SEM images of (a and b) MnO_x(0.36)-E and (c and d) MnO_x(0.36)-P nanorods catalysts.

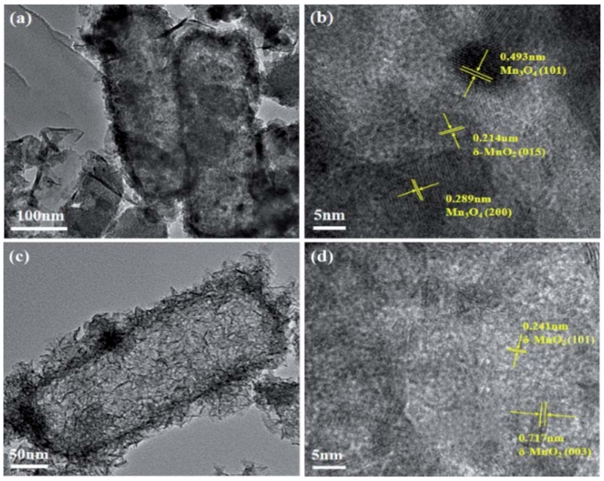

Fig. 3 TEM and HRTEM images of (a and b) MnO_x(0.36)-E and (c and d) MnO_x(0.36)-P nanorods.

The HRTEM images of the two catalysts are shown in Fig. 3b and d. The HRTEM image of MnO_x(0.36)-E nanorods reveals the visible lattice fringes with an interplanar spacing of 0.214, 0.289 and 0.493 nm, which can be assigned to the (015) plane of birnessite-type MnO_2 (δ-MnO_2), (200) and (101) planes of Mn_3O_4, respectively. These data suggests that Mn_3O_4 and δ-MnO_2 coexist on the surface of MnO_x(0.36)-E nanorods. However, for MnO_x(0.36)-P nanorods, the lattice fringes with an interplanar spacing of 0.241 and 0.717 nm can be observed, which can be assigned to the (101) and (003) crystal planes of δ-MnO_2, respectively.

3.2 NO removal activities

Fig. 4 exhibits the NO removal activities of MnO_x nanorods catalysts obtained by the two different methods. It can be seen that the catalysts preparation method has significant effect on the NO removal activity. As shown in Fig. 4a, MnO_x(0.36)-P and MnO_x(0.72)-P nanorods catalysts exhibit higher NO removal activity, above 94% of NO conversions can be achieved at temperatures of 100–200 °C. Especially in the low temperature range of 100–180 °C, they maintain about 98% NO conversions. For MnO$_x$(0.18)-P nanorods, it shows relatively low NO removal activity, but the maximum NO conversion is still up to 92% at 160 °C. From Fig. 4b, it can be observed that MnO$_x$(0.18)-E and MnO$_x$(0.36)-E nanorods catalysts exhibit relatively high NO removal activity. NO conversions of the two catalysts at 100 °C is approximately 70%, and they reach more than 90% in the temperature range of 140–240 °C. For MnO$_x$(0.72)-E nanorods, it shows relatively low NO removal activity below 200 °C, but it reaches a maximum value (above 90%) at 240 °C. For all MnO$_x$ nanorods, NO conversions decline at relative higher temperatures, which might be explained that partial NH_3 reductant is oxidized into NO.[18] Fig. 4c and d compare the NO removal activities over the MnO$_x$ nanorods catalysts obtained by the two different methods. Compared with MnO$_x$(0.36)-E nanorods, MnO$_x$(0.36)-P nanorods exhibits higher NO conversion in the low temperature range of 100–160 °C. For the catalyst with higher Mn loading, NO conversion of MnO$_x$(0.72)-P nanorods at low temperatures of 100–180 °C is significantly higher than that of MnO$_x$(0.72)-E nanorods. These results clearly indicate that the catalyst prepared by redox precipitation method shows much higher NO removal activity at the low temperature range (below 200 °C) than that prepared by solvent evaporation method, which may result from the unique morphology of MnO$_x$-P nanorods.

3.3 XRD

To further investigate the crystal phase composition of MnO$_x$ nanorods catalysts obtained by different methods, XRD patterns were characterized, and the results are shown in Fig. 5. The XRD pattern of MnO$_x$(0.36)-E nanorods displays the characteristic diffraction peaks located at $2\theta = 18.0°$, 28.9°, 32.4°, 36°, 44.4°, 58.5°, 59.9° and 64.7°, which can be indexed as the (101), (112), (103), (211), (220), (321), (224) and (400) crystal planes of Mn_3O_4 with a spinel structure (JCPDS card no. 24-0734), respectively.[19] And it can also be observed that the diffraction peaks at 12.3°, 24.8°, 36.9° and 42.2° are ascribed to the (003), (006), (101), and (015) crystal planes of δ-MnO_2 (JCPDS card no. 52-0556), respectively.[20] For MnO$_x$(0.36)-P nanorods, the diffraction peaks at 12.3°, 24.8°, 36.9°, 42.2°, and 66.3° are assigned to the (003), (006), (101), (015), and (113) planes of δ-MnO_2 crystalline phase. These data is consistent with the observation using HRTEM. It is worth noting that the diffraction peaks of MnO$_x$ on MnO$_x$(0.36)-P nanorods become broader and the intensities of the peaks become much weaker than those of MnO$_x$(0.36)-E nanorods, suggesting the smaller size of crystal particle and lower crystallinity of MnO$_x$. It has been widely demonstrated that amorphous phase of manganese oxides usually exhibits higher catalytic activity for SCR of NO

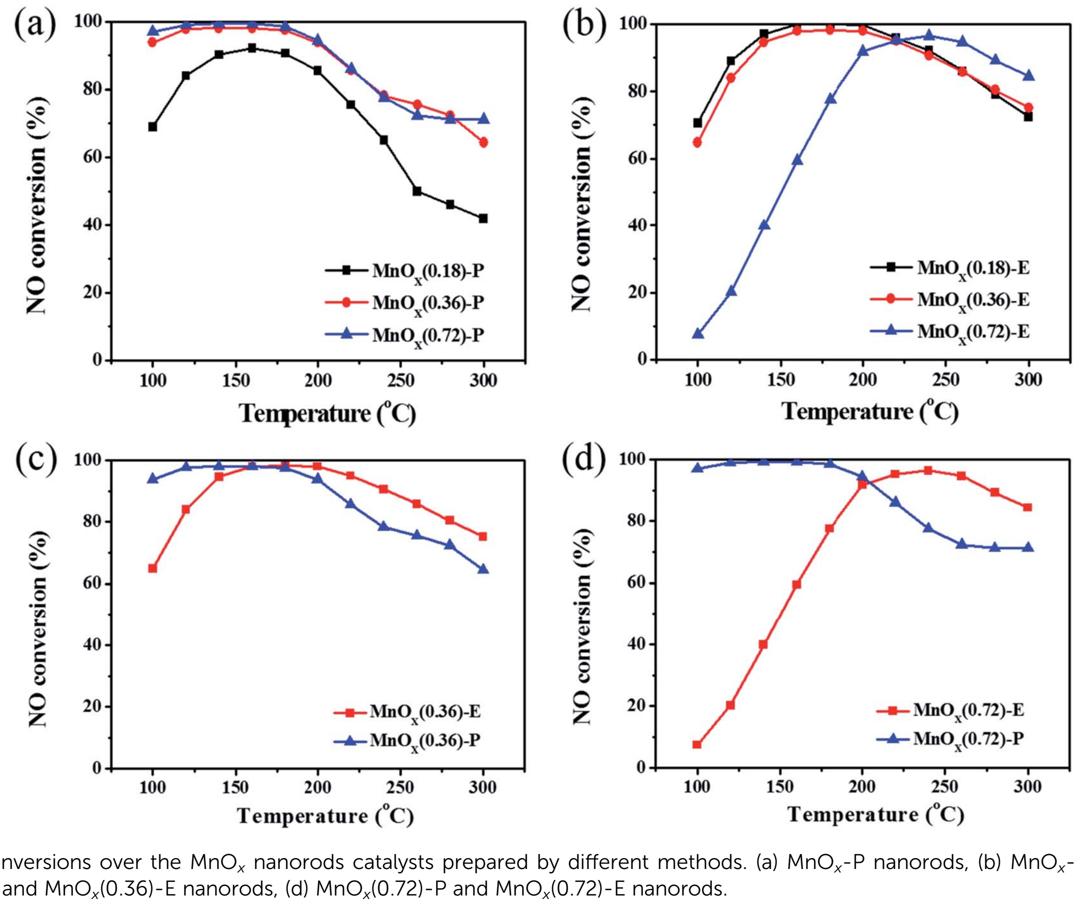

Fig. 4 NO conversions over the MnO$_x$ nanorods catalysts prepared by different methods. (a) MnO$_x$-P nanorods, (b) MnO$_x$-E nanorods, (c) MnO$_x$(0.36)-P and MnO$_x$(0.36)-E nanorods, (d) MnO$_x$(0.72)-P and MnO$_x$(0.72)-E nanorods.

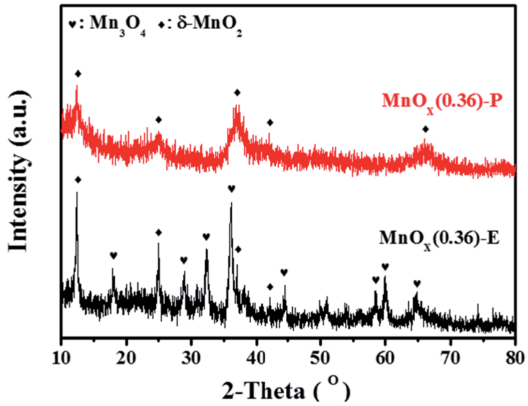

Fig. 5 XRD patterns of the different samples.

than crystal manganese oxides.[21] Based on these results, it can be concluded that the improved dispersion of MnO_x species is obtained by the redox precipitation method, which contributes to the excellent SCR activity of MnO_x(0.36)-P nanorods, as evidenced by the results of activity evaluation presented in Fig. 4.

3.4 Pore structure analysis

The pore structure characterizations of the MnO_x nanorods catalysts obtained by different methods are analyzed by N_2 adsorption–desorption isotherms. As presented in Fig. 6a, MnO_x(0.36)-E nanorods exhibits a typical type-IV isotherm with a hysteresis loop at the relative pressure (P/P_0) of 0.4–0.9, indicating the presence of mesopores. For MnO_x(0.36)-P nanorods, the isotherm still belongs to the type-IV isotherm with an obvious hysteresis loop at P/P_0 of 0.8–1.0, suggesting that the catalyst has characteristic of mesoporous material (Fig. 6c). Their pore sizes are further analyzed, as shown in Fig. 6b and d, respectively. The pore size distribution curve of MnO_x(0.36)-E nanorods shows the coexistence of micropores and mesopores, and its pore size distributes in the range of 0.6–4 nm. MnO_x(0.36)-P nanorods exhibits a wider pore size distribution and a larger number of mesopores in the range of 4–28 nm can be also observed. Moreover, the pore parameters of the samples are listed in Table 1. It can be observed that the S_{BET} for MnO_x(0.36)-P and MnO_x(0.36)-E nanorods is 151 m^2 g^{-1} and 272 m^2 g^{-1}, respectively. The S_{BET} values of these MnO_x nanorods catalysts are much larger than those of carrier-free MnO_x-based catalysts as previously reported,[15,22] which may result from the highly porous structure of SiO_2 nanorods template and/or the accumulation of the nanoparticles. It is worth pointing out that the V_{total} of MnO_x(0.36)-P nanorods (0.61 cm^3 g^{-1}) is significantly higher than that of MnO_x(0.36)-E nanorods (0.31 cm^3 g^{-1}), which may be due to its flower-like structure, as demonstrated by the SEM results (Fig. 2c and d). Additionally, the pore volume of MnO_x(0.36)-P nanorods at smaller pore sizes (<4 nm) decreases obviously, and the pore volume at larger pore sizes (5–28 nm) increases greatly, indicating that there exists more mesoporous structure in MnO_x(0.36)-P nanorods. Thus, such rich mesoporous structure with high pore volume of MnO_x(0.36)-P nanorods may be favorable for exposure of more active sites of MnO_x and the adsorption of reactant molecules, leading to the excellent SCR activity at the low temperatures (below 200 °C).

3.5 XPS characterization

To further determine the surface chemical states of elements in MnO_x nanorods catalysts, the XPS measurement was carried out and the results are presented in Fig. 7. The relative atomic ratios of Mn and O elements are summarized in Table 2. As displayed Fig. 7a, the Mn 2p spectrum of MnO_x(0.36)-E nanorods exhibits two main peaks with binding energies of 653.8 eV and 642.3 eV, which represents Mn $2p_{1/2}$ and Mn $2p_{3/2}$, respectively. The Mn $2p_{3/2}$ spectrum can be fitted into three characteristic peaks at 641.0–642.0 eV, 642.2–642.5 eV and 642.9–643.7 eV, corresponding to Mn^{2+}, Mn^{3+}, and Mn^{4+}, respectively.[23,24] These data suggests that Mn^{4+}, Mn^{3+} and Mn^{2+} manganese oxide phases coexist on the surface of MnO_x(0.36)-E nanorods. For MnO_x(0.36)-P nanorods, the binding energies of Mn $2p_{1/2}$ and Mn $2p_{3/2}$ are located at 653.9 eV and 642.2 eV, respectively. The binding energy separation between these two peaks is 11.7 eV, which is in accordance with previously reported results of MnO_2,[25,26] indicating that the valence of Mn element is very close to 4 in MnO_x(0.36)-P nanorods. Moreover, the Mn $2p_{3/2}$ spectrum is fitted into two peaks, which are attributed to Mn^{3+} (642.1 eV) and Mn^{4+} (643.5 eV), respectively. These results further demonstrate that MnO_2 is the main manganese oxide in MnO_x(0.36) nanorods, which is in accordance with the XRD result. The relative ratio of different oxidation state of manganese species can be calculated by the area ratio of Mn^{2+}, Mn^{3+} and Mn^{4+} species, as shown in Table 2. The percentage of Mn^{4+}/Mn^{n+} on MnO_x(0.36)-P nanorods (50.8%) is greatly higher than that on MnO_x(0.36)-E nanorods (35.7%). As literature reported,[27,28] manganese species with higher oxidation state are preferable for oxidation reactions over the manganese-based catalysts. It has been confirmed that Mn^{4+} species are beneficial to promote the low-temperature SCR activity, due to the enhancement of oxidation of NO to NO_2.[29,30] Therefore, the higher percentage of Mn^{4+} on MnO_x(0.36)-P nanorods results in the increased SCR activity at the low temperatures of 100–160 °C.

As shown in Fig. 7b, the O 1s XPS spectra can be fitted into two peak. The peak located at 529.5–530.2 eV can be assigned to the lattice oxygen (O^{2-}) (denoted as O_α), while the peak located at 531.2–532.0 eV is assigned to the chemisorbed oxygen, such as O^- or O_2^{2-} (denoted as O_β).[31] The relative concentrations of O_α and O_β can be determined from the area ratio of $O_\alpha/(O_\alpha + O_\beta)$ and $O_\beta/(O_\alpha + O_\beta)$, respectively. As illustrated by Table 2, the ratio of $O_\beta/(O_\alpha + O_\beta)$ is 49.3% and 38.6% for MnO_x(0.36)-E and MnO_x(0.36)-P nanorods, respectively, which is higher than the data previously reported for MnO_2 nanorods (36.7%) and MnO_x/TiO_2-GE (19.9%).[32,33] It has been widely reported that the surface chemisorbed oxygen species (O_β) are more active than the lattice oxygen species (O_α) in oxidation reactions because of their higher mobility, which may easily exchange with oxygen in the gas phase or oxygen molecules absorbed on catalyst surface, thus acting as the supplement of lattice oxygen.[34–36] Moreover,

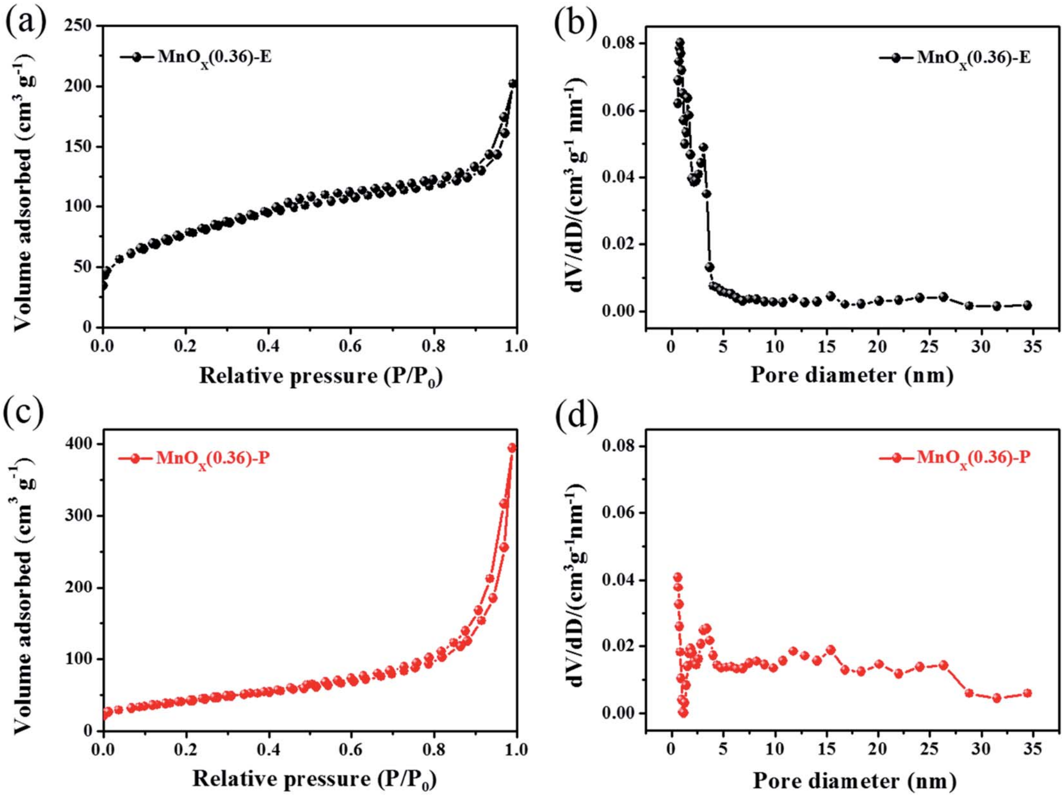

Fig. 6 N_2 adsorption–desorption isotherms and corresponding pore size distributions of (a and b) MnO_x(0.36)-E and (c and d) MnO_x(0.36)-P nanorods.

Table 1 Pore parameters of MnO_x nanorods catalysts obtained by different methods[a]

Sample	S_{BET} ($m^2\ g^{-1}$)	V_{total} ($cm^3\ g^{-1}$)	Average pore size (nm)
MnO_x(0.36)-P	151	0.61	3.5
MnO_x(0.36)-E	272	0.31	4.6

[a] S_{BET}: BET specific surface area; V_{total}: total pore volume.

the higher concentration of O_β is advantageous to the improvement of oxidation of NO to NO_2, which facilitates the "fast SCR" reaction ($4NH_3 + 2NO + 2NO_2 \rightarrow 4N_2 + 6H_2O$),[37–39] resulting in the enhancement of catalytic activity. Thus, the relative high concentration of surface chemisorbed oxygen in MnO_x(0.36)-E and MnO_x(0.36)-P nanorods is favorable for achieving high SCR activity. The above XPS results demonstrate that the high concentration of Mn^{4+} species plays an important role in the low-temperature SCR activity of MnO_x(0.36)-P nanorods.

3.6 NH_3-TPD

It is generally known that the adsorption and oxidation of NH_3 on the surface acid sites of catalyst are considered to be a key step in the NH_3-SCR reaction. NH_3-TPD experiments were performed to determine the surface acidity of the obtained catalysts, and the results are shown in Fig. 8 and Table 3. It is found

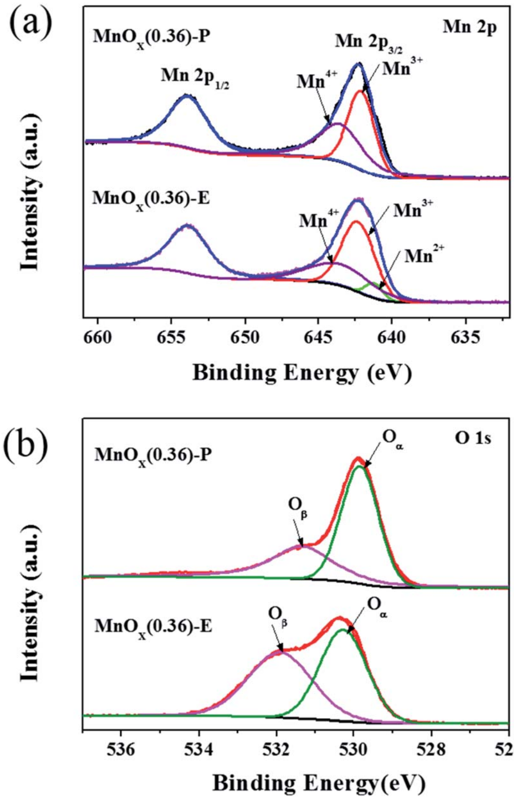

Fig. 7 XPS spectra for Mn 2p (a) and O 1s (b) of the different MnO_x nanorods catalysts.

Table 2 The relative atomic ratios of the different MnO_x nanorods catalysts

	X_{Mn} (%)			X_O (%)	
Sample	Mn^{2+}	Mn^{3+}	Mn^{4+}	O_α	O_β
MnO_x(0.36)-P	0	49.2	50.8	61.4	38.6
MnO_x(0.36)-E	6.4	57.9	35.7	50.7	49.3

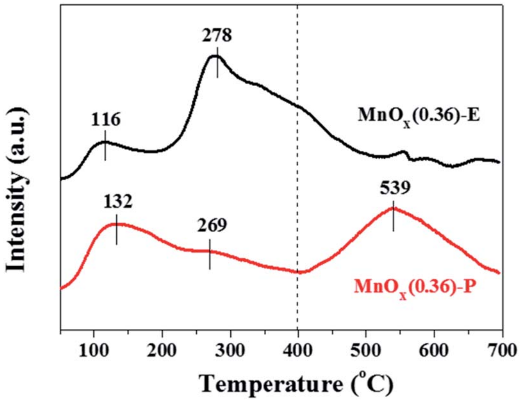

Fig. 8 NH_3-TPD profiles of the different MnO_x nanorods catalysts.

Table 3 The amount of surface acids over the different catalysts

	Peak temperature (°C)			Acid amount (a.u. g^{-1})		
Sample	T_1[a]	T_2	T_3	S_1[b]	S_2	S_3
MnO_x(0.36)-P	132	269	539	30.3	28.9	56.7
MnO_x(0.36)-E	116	278	—	17.0	86.8	—

[a] The desorption peak at temperature. [b] The area of desorption peak.

that MnO_x(0.36)-E nanorods exhibits two obvious desorption peaks located at the temperature range of 50–180 °C (labeled as peak 1) and 190–400 °C (labeled as peak 2). And no visible desorption peaks above 400 °C can be observed. For MnO_x(0.36)-P nanorods, besides the two desorption peaks located at 50–400 °C, another desorption peak at 410–690 °C (labeled as peak 3) is also observed. The peaks 1 and 2 are ascribed to NH_3 desorption from the weak acid sites, and peak 3 is assigned to the strong acid sites. It is generally accepted that the area of NH_3 desorption peak is proportional to the amount of acid sites. As listed in Table 3, the desorption peak area of strong acid sites over MnO_x(0.36)-P nanorods significantly enhances compared with MnO_x(0.36)-E nanorods, indicating that a large amount of strong acid sites exist on its surface. Based on the above results, MnO_x(0.36)-P nanorods has stronger surface acidity, especially there are more amount of strong acid sites on it, which contributes to enhancement of NH_3 adsorption and oxidation on the catalyst surface, leading to the excellent low-temperature SCR activity of MnO_x(0.36)-P nanorods.

4. Conclusions

A series of MnO_x nanorods catalysts using porous SiO_2 nanorods as template were synthesized through two different preparation methods. The obtained MnO_x-P nanorods catalyst prepared by redox precipitation method exhibits higher NO removal activity at low temperatures (lower than 200 °C) in comparison to MnO_x-E nanorods. About 98% NO conversion is achieved over MnO_x(0.36)-P nanorods in the low temperature range of 100–180 °C. The reason is mainly attributed to its unique flower-like morphology and mesoporous structures with high pore volume. Furthermore, there are the lower crystallinity of MnO_x, higher percentage of Mn^{4+} species and a large amount of strong acid sites on the surface of MnO_x(0.36)-P nanorods. These factors result in its excellent low-temperature SCR activity.

Conflicts of interest

There are no conflicts to declare.

Acknowledgements

The authors gratefully acknowledge the financial supports from the National Natural Science Foundation of China (No. 51472086, 51002051, 22075081, 20806024), and the Natural Science Foundation of Shanghai City (12ZR1407200).

Notes and references

1 S. B. Kristensen, A. J. Kunov-Kruse, A. Riisager, S. B. Rasmussen and R. Fehrmann, *J. Catal.*, 2011, **284**, 60–67.
2 P. Forzatti, *Catal. Today*, 2000, **62**, 51–65.
3 J. W. Shi, Z. Y. Fan, C. Gao, G. Gao, B. R. Wang, Y. Wang, C. He and C. M. Niu, *ChemCatChem*, 2018, **10**, 2833–2844.
4 J. Liu, Y. J. Wei, P. Z. Li, P. P. Zhang, W. Su, Y. Sun, R. Q. Zou and Y. L. Zhao, *ACS Catal.*, 2018, **8**, 3865–3874.
5 Y. R. Shi, X. L. Tang, H. H. Yi, F. Y. Gao, S. Z. Zhao, J. G. Wang, K. Yang and R. C. Zhang, *Ind. Eng. Chem. Res.*, 2019, **58**, 3606–3617.
6 C. Fang, D. S. Zhang, S. X. Cai, L. Zhang, L. Huang, H. R. Li, P. Maitarad, L. Y. Shi, R. H. Gao and J. P. Zhang, *Nanoscale*, 2013, **5**, 9199–9207.
7 R. H. Wang, Z. F. Hao, Y. Li, G. Q. Liu, H. Zhang, H. T. Wang, Y. G. Xia and S. H. Zhan, *Appl. Catal., B*, 2019, **258**, 117983.
8 F. Kapteijn, L. Singoredjo, A. Andreini and J. A. Moulijn, *Appl. Catal., B*, 1994, **3**, 173–189.
9 X. Y. Wang, K. Zhang, W. T. Zhao, Y. Y. Zhang, Z. X. Lan, T. H. Zhang, Y. H. Xiao, Y. F. Zhang, H. Z. Chang and L. L. Jiang, *Ind. Eng. Chem. Res.*, 2017, **56**, 14980–14994.
10 X. J. Yao, L. Chen, J. Cao, F. M. Yang, W. Tan and L. Dong, *Ind. Eng. Chem. Res.*, 2018, **57**, 12407–12419.
11 Z. H. Lian, W. P. Shan, Y. Zhang, M. Wang and H. He, *Ind. Eng. Chem. Res.*, 2018, **57**, 12736–12741.
12 S. H. Zhan, H. Zhang, Y. Zhang, Q. Shi, Y. Li and X. J. Li, *Appl. Catal., B*, 2017, **203**, 199–209.
13 C. L. Xiao, X. Y. Zhang, T. Mendes, G. P. Knowles, A. Chaffee and D. R. MacFarlane, *J. Phys. Chem. C*, 2016, **120**, 23976–23983.

14 C. Fang, L. Y. Shi, H. R. Li, L. Huang, J. P. Zhang and D. S. Zhang, *RSC Adv.*, 2016, **6**, 78727–78736.

15 J. S. Gao, Y. L. Han, J. C. Mu, S. C. Wu, F. Tan, Y. Shi and X. Y. Li, *J. Colloid Interface Sci.*, 2018, **516**, 254–262.

16 W. Tian, H. S. Yang, X. Y. Fan and X. B. Zhang, *J. Hazard. Mater.*, 2011, **188**, 105–109.

17 W. Q. Yao, C. J. Chu, W. Z. Zheng, L. Zhan and Y. L. Wang, *J. Mater. Chem. A*, 2018, **6**, 18191–18205.

18 T. S. Park, S. K. Jeong, S. H. Hong and S. C. Hong, *Ind. Eng. Chem. Res.*, 2001, **40**, 4491–4495.

19 Y. F. Jian, M. D. Ma, C. W. Chen, C. Liu, Y. K. Yu, Z. P. Hao and C. He, *Catal. Sci. Technol.*, 2018, **8**, 3863–3875.

20 G. Zhu, L. J. Deng, J. F. Wang, L. P. Kang and Z. H. Liu, *Colloids Surf., A*, 2013, **434**, 42–48.

21 G. Gao, J. W. Shi, C. Liu, C. Gao, Z. Y. Fan and C. M. Niu, *Appl. Surf. Sci.*, 2017, **411**, 338–346.

22 S. H. Zhan, D. D. Zhu, M. Y. Qiu, H. B. Yu and Y. Li, *RSC Adv.*, 2015, **5**, 29353–29361.

23 Z. Y. Fan, J. W. Shi, C. Gao, G. Gao, B. R. Wang and C. M. Niu, *ACS Appl. Mater. Interfaces*, 2017, **9**, 16117–16127.

24 C. L. Li, X. L. Tang, H. H. Yi, L. F. Wang, X. X. Cui, C. Chu, J. Y. Li, R. C. Zhang and Q. J. Yu, *Appl. Surf. Sci.*, 2018, **428**, 924–932.

25 X. Wang, Y. Y. Zheng, Z. Xu, Y. Liu and X. L. Wang, *Catal. Sci. Technol.*, 2014, **4**, 1738–1741.

26 E. Miniach, A. Sliwak, A. Moyseowicz, L. Fernández-Garcia, Z. González, M. Granda, R. Menendez and G. Gryglewicz, *Electrochim. Acta*, 2017, **240**, 53–62.

27 X. F. Tang, Y. G. Li, X. M. Huang, Y. D. Xu, H. Q. Zhu, J. G. Wang and W. J. Shen, *Appl. Catal., B*, 2006, **62**, 265–273.

28 Q. Shen, L. Y. Zhang, N. N. Sun, H. Wang, L. S. Zhong, C. He, W. Wei and Y. H. Sun, *Chem. Eng. J.*, 2017, **322**, 46–55.

29 B. X. Shen, Y. Y. Wang, F. M. Wang and T. Liu, *Chem. Eng. J.*, 2014, **236**, 171–180.

30 L. Zhang, D. S. Zhang, J. P. Zhang, S. X. Cai, C. Fang, L. Huang, H. R. Li, R. H. Gao and L. Y. Shi, *Nanoscale*, 2013, **5**, 9821–9829.

31 K. W. Zha, S. X. Cai, H. Hu, H. R. Li, T. T. Yan, L. Y. Shi and D. S. Zhang, *J. Phys. Chem. C*, 2017, **121**, 25243–25254.

32 Y. Li, Y. P. Li, Y. Wan, S. H. Zhan, Q. X. Guan and Y. Tian, *RSC Adv.*, 2016, **6**, 54926–54937.

33 X. N. Lu, C. Y. Song, S. H. Jia, Z. S. Tong, X. L. Tang and Y. X. Teng, *Chem. Eng. J.*, 2015, **260**, 776–784.

34 F. D. Liu, W. P. Shan, Z. H. Lian, L. J. Xie, W. W. Yang and H. He, *Catal. Sci. Technol.*, 2013, **3**, 2699–2707.

35 P. Sun, R. T. Guo, S. M. Liu, S. X. Wang, W. G. Pan and M. Y. Li, *Appl. Catal., A*, 2017, **531**, 129–138.

36 L. Chen, X. X. Wang, Q. L. Cong, H. Y. Ma, S. J. Li and W. Li, *Chem. Eng. J.*, 2019, **369**, 957–967.

37 F. D. Liu, H. He, Y. Ding and C. B. Zhang, *Appl. Catal., B*, 2009, **93**, 194–204.

38 T. Boningari, P. R. Ettireddy, A. Somogyvari, Y. Liu, A. Vorontsov, C. A. McDonald and P. G. Smirniotis, *J. Catal.*, 2015, **325**, 145–155.

39 F. Y. Gao, X. L. Tang, H. H. Yi, J. Y. Li, S. Z. Zhao, J. G. Wang, C. Chu and C. L. Li, *Chem. Eng. J.*, 2017, **317**, 20–31.